



Article

Surface Photonic Crystal Engineering of a Multi-Mode VCSEL for a Bit-Loaded Broadband QAM-OFDM Data Link at 99 Gbit/s

Yu-Hong Lin ¹, Chih-Hsien Cheng ² , Cheng-Ting Tsai ¹, Wei-Li Wu ¹, Kent D. Choquette ³ and Gong-Ru Lin ^{1,4,*} 

¹ Graduate Institute of Photonics and Optoelectronics and the Department of Electrical Engineering, National Taiwan University, Taipei 10617, Taiwan

² Optical Access Technology Laboratory, Photonic ICT Research Center, Network Research Institute, National Institute of Information and Communications Technology, Koganei 184-8795, Tokyo, Japan

³ Department of Electrical and Computer Engineering, University of Illinois at Urbana-Champaign, Urbana, IL 61801, USA

⁴ NTU-Tektronix Joint Research Center, National Taiwan University, Taipei 10617, Taiwan

* Correspondence: grlin@ntu.edu.tw; Tel.: +886-2-33663700 (ext. 6519)

Abstract: Bit-loaded quadrature amplitude modulation-orthogonal frequency division multiplexing (QAM-OFDM) encoding and photonic-crystal-engineered multi-mode vertical-cavity surface-emitting lasers (MM-VCSELs) transmission performance are analyzed. Two different surface photonic-crystal designs are used to configure the core and cladding regions of MM-VCSELs, producing continuous-wave and digital-encoding outputs. These outputs are combined with the end-face-flattened OM5 multi-mode fiber (MMF) for 100 m short-reach transmission. The photonic-crystal (PhC) structure exhibits a spatial mode-filtering ability, supporting few or single-mode outputs from the MM-VCSEL. This helps reduce the modal dispersion during OM5-MMF transmission of the encoded data. Comparing the original MM-VCSEL with two different surface-photonic-crystal-configured MM-VCSELs, the allowable bit-loaded QAM-OFDM data rate can be increased from 60.7 (for the VCSEL without the PhC structure) to 85/65 Gbit/s (for the PhC VCSELs with 2-layer PhC structures in the cladding layer and the ones with a 1-layer PhC structure in the core layer and 2-layer PhC structures in the cladding layer, respectively) under back-to-back (BtB) encoding and enable the 100 m OM5-MMF transmission to increase from 58.5 (for the VCSEL without the PhC structure) to 81.2/64.6 Gbit/s (for the PhC VCSELs with 2-layer PhC structures in the cladding layer and the ones with a 1-layer PhC structure in the core layer and 2-layer PhC structures in the cladding layer), respectively. Furthermore, by comparing the 7°-titled and 0°-normalized vertical coupling conditions, it can be observed that the purely normalized vertical coupling can collect more output power, resulting in an improved signal-to-noise ratio. This significantly increases the allowable error-free data rate from 85 to 98.9 Gbit/s in the BtB case and from 81.2 Gbit/s to 95.3 Gbit/s in the 100 m OM5-MMF case.

Keywords: vertical cavity surface-emitting laser (VCSEL); photonic crystals; 400G; intra-data-center



Citation: Lin, Y.-H.; Cheng, C.-H.; Tsai, C.-T.; Wu, W.-L.; Choquette, K.D.; Lin, G.-R. Surface Photonic Crystal Engineering of a Multi-Mode VCSEL for a Bit-Loaded Broadband QAM-OFDM Data Link at 99 Gbit/s. *Photonics* **2023**, *10*, 549. <https://doi.org/10.3390/photonics10050549>

Received: 28 February 2023

Revised: 19 April 2023

Accepted: 2 May 2023

Published: 9 May 2023



Copyright: © 2023 by the authors. Licensee MDPI, Basel, Switzerland. This article is an open access article distributed under the terms and conditions of the Creative Commons Attribution (CC BY) license (<https://creativecommons.org/licenses/by/4.0/>).

1. Introduction

Multi-mode vertical-cavity surface-emitting lasers (MM-VCSELs) are now widely used in data-center network architectures [1–10]. To facilitate faster data streaming and exchange for high-speed cloud transportation, various modifications have been made to the MM-VCSEL structure to improve its analog modulation and digital-encoding capacities [11–20]. Among these approaches, scaling down the emission area is the commonly used scheme for shortening the RC response to enhance the data-switching speed of MM-VCSELs. However, this mode-number-confined design reduces the lasing power and enlarges the differential resistance to concurrently reduce modulation efficiency and the signal-to-noise ratio (SNR) [21,22]. Alternative methods have emerged to improve the modulation bandwidth, such as photonic-crystal (PhC) engineering of the MM-VCSEL cavity to control

mode numbers [23–25], using zinc-diffusion in distributed Bragg reflectors (DBRs) for impedance matching [26–28], applying surface overlayer coating or chemical processing to reduce capacitance [29–31], etc. Additionally, the coupling efficiency of MM-VCSEL output has been enhanced using MMF fibers with either flattened and lensed end-faces under different tilting angles or coupling schemes. These developments highlight the trade-off between the small-signal bandwidth and the SNR in MM-VCSELs under direct modulation, which gradually leads to the state-of-the-art design of MM-VCSELs for 100-Gbit/s applications.

To increase the bit rate per channel in data centers, various digital formats have successfully encoded VCSEL to improve spectral usage efficiency within a finite bandwidth. In 2013, Tan et al. encoded an 850 nm VCSEL transmitter with an additional PhC structure for carrying the on-off keying (OOK) data at 25-Gbit/s after 1 km MMF transmission [17]. In 2015, Kuchta et al. modulated the 850-nm VCSEL with non-return-to-zero on-off-keying (NRZ-OOK) data at 71-Gbit/s for 7 m MMF transmission [32]. In contrast to the NRZ-OOK data format, 4-/8-level pulse amplitude modulation (PAM-4/PAM-8) data formats were also used to encode the 850-nm VCSEL to demonstrate 70-/56-Gbit/s transmission links over a 50 m OM4 MMF [33]. Lavrencik et al. achieved up to 107-Gbit/s PAM-4 transmission in a 105 m MMF link using 850/940 nm VCSELs [34]. Furthermore, the quadrature amplitude modulation orthogonal frequency division multiplexing (QAM-OFDM) data format, which has higher spectral usage efficiency than other formats, was also employed to overcome the finite encoding bandwidth of the VCSEL [35,36]. Kao et al. preliminarily reported 100 m OM4 MMF transmission at a data rate of 80 Gbit/s via directly modulating the VCSEL with 16-QAM-OFDM data [21]. However, the transmission performance of the QAM-OFDM data format carried by the multi-mode VCSEL with versatile PhC structures has seldom been discussed.

This work focuses on further engineering an MM-VCSEL at 850 nm using two designs of surface PhC structures for its core and cladding regions. The emission aperture of these MM-VCSELs is confined using proton bombardment for distinct current-blocking confinement. The specific core/cladding PhC designs favor controlling the modal field and the modal number of MM-VCSELs without sacrificing their lasing performance. The surface photonic-crystal structures are designed with different pitch periods and hole diameters for the MM-VCSEL core and cladding, which are post-processed within the proton-bombardment-confined mesa of the MM-VCSELs via ionic plasma etching. To analyze the performance of these PhC-engineered MM-VCSELs, we employed the OM5-MMF as the uncollimated coupler for these devices to perform bit-loaded QAM-OFDM back-to-back encoding and 100 m OM5-MMF transmission. Three types of core-/cladding unprocessed and photonic-crystal-engineered MM-VCSELs were analyzed by comparing their power-to-current and voltage-to-current curves, lasing optical spectra and modulation response, and broadband bit-loaded QAM-OFDM encoding performances to obtain the optimized design. Two kinds of vertical coupling schemes with adjustment to the tilting angle of the uncollimated end-face-flattened OM5-MMF butt coupler between 0 and 7 degrees are compared to improve the bit-loaded QAM-OFDM data transmission and receiving performances of the surface-PhC-engineered MM-VCSELs. These schemes help to improve the allowable broadband QAM-OFDM encoding bandwidth, the decoding error vector magnitude of the constellation plot, the receiving SNR of QAM-OFDM data, and the calculated bit error ratio (BER) after transmission. To overcome the roll-off (unflattened) power-to-frequency response of the PhC VCSELs and the dispersion-degraded MMF transmission, the pre-leveling and bit-loading algorithms were introduced to improve the SNR performance of the QAM-OFDM data.

2. Experimental Setup

2.1. Device Design and Fabrication of the PhC VCSEL

Figure 1a shows the cross-section structure of the PhC VCSEL. A similar device design has been previously reported [37]. In this study, the PhC VCSEL device was fabricated on

a GaAs substrate. Initially, an n-type DBR mirror with 36-pair $\text{Al}_{0.1}\text{Ga}_{0.9}\text{As}/\text{Al}_{0.9}\text{Ga}_{0.1}\text{As}$ layers was formed. All of the DBR layers had quarter-wave thickness except when terminating the last high index layer with a thickness of $3/4$ lambda to ensure the constructive interference of reflected waves within specific wavelength bands. After the n-type DBR fabrication, the active gain region of the PhC VCSEL was deposited on top of the n-type DBR layer. This region consisted of 3-pair unstrained GaAs quantum wells and 4-layer $\text{Al}_{0.3}\text{Ga}_{0.7}\text{As}$ barriers sandwiched between 2-layer $\text{Al}_{0.6}\text{Ga}_{0.4}\text{As}$ cladding. This configuration aimed to control the central point of the gain spectrum at 850 nm. Finally, a p-type DBR mirror with 23-pair $\text{Al}_{0.10}\text{Ga}_{0.90}\text{As}/\text{Al}_{0.90}\text{Ga}_{0.10}\text{As}$ layers was formed to fabricate the whole VCSEL.

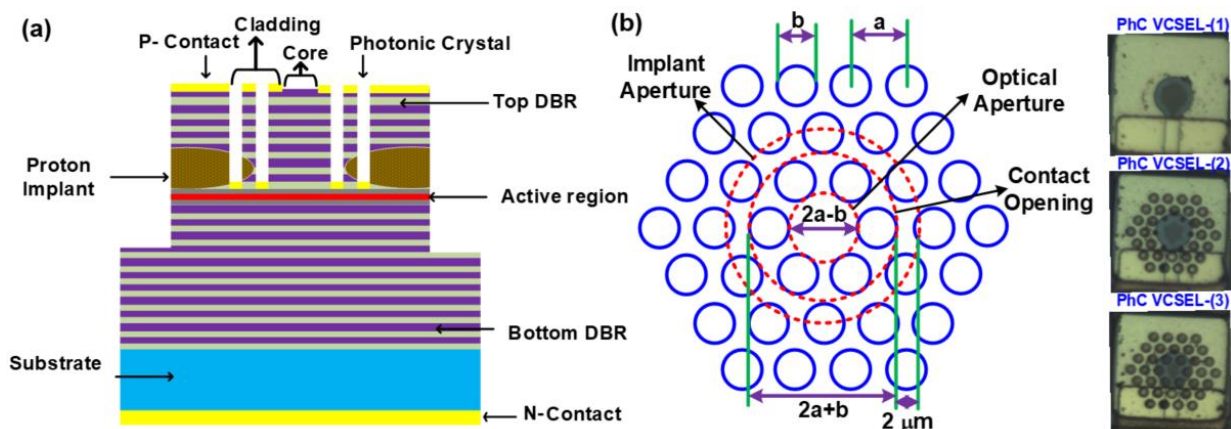


Figure 1. (a) Cross-section of the 22DD structure and (b) diagram of the PhC design in the PhC VCSEL and the top-view images for the proton-implanted PhC VCSEL.

In this work, the dry-etching process was also utilized to fabricate the PhC structure [30]. Before the dry-etching process, a SiO_2 mask was formed upon the p-type DBR mirror. Then, the patterns of the mesa and PhC were defined by the photolithography process. These patterns were transferred onto the SiO_2 layer by the CF_4 reactive-ion etching (RIE) process. Before proton implantation, the circular aperture was defined by the photolithography process. Proton implantation technology with an energy of 330 keV and a dose concentration of $5 \times 10^{12} \text{ cm}^{-2}$ was used to form a high-resistivity insulating area around the circular core deep within the VCSEL cavity to define the aperture. After proton implantation, the patterns of the mesa and PhC were etched via the SiCl_4/Ar inductively coupled plasma RIE (ICP-RIE) process. The etching depth was controlled at 90–100% of the DBR thickness during the ICP-RIE process. For the calibration in the previous work [30], the etching depth was determined by counting the individual DBR layers in the scanning electron micrograph image. More importantly, this process had to avoid damaging the active gain region to prevent gain degradation and heat accumulation. Over-etching could lead to non-radiative Auger recombination and decreased quantum efficiency. Next, the CF_4 RIE process removed the SiO_2 mask for coating the metal contacts. Finally, electron-beam physical vapor deposition deposited the p-type Ti/Au and n-type AuGe/Ni/Au contacts. The metal contacts of the VCSEL were extended to a ground-signal-ground (GSG) coplanar contact for high-speed measurement. Based on the structural design of the PhC in the PhC VCSEL from previous work (Figure 1b) [37], the design parameters of three PhC VCSELs are listed in Figure 1b and Table 1. Comparing different PhC designs, different period hexagonally aligned arrays of circular holes were used in both the core and cladding regions. The a , b , and b/a parameters denote the hole pitch, hole diameter, and pitch ratio, respectively. For the PhC VCSEL-(1), no PhC crystal structures exist in the core and cladding regions of the original VCSELs. When the a , b , and b/a parameters for the PhC VCSEL-(1) are set at 5 μm , 3 μm , and 0.6, respectively, the implant and optical aperture diameters are 17 μm and 7 μm , respectively. In addition, the metal opening diameter

is also set at 13 μm . For the PhC VCSEL-(2), the device has no PhC pattern in the core region and 2-period PhC regions in the cladding region with a , b , and (b/a) parameters of 3.5 μm , 2.45 μm , and 0.7, respectively. For the fixed a , b , and (b/a) parameters, the metal opening, implant aperture, and optical aperture diameters changed to 9.45 μm , 13.45 μm , and 4.55 μm , respectively. The inner hole diameter was decreased to 1.75 μm . For the PhC VCSEL-(3), the device inserts an additional 1-period PhC pattern in the core region and maintains 2-period PhC patterns in the cladding compared to the PhC VCSEL-(2). For the PhC VCSEL-(3), the a , b , and b/a parameters were varied at 4.5 μm , 3.15 μm , and 0.7, respectively. Therefore, the metal opening, implant aperture, and optical aperture diameters changed to 12.15 μm , 16.15 μm , and 5.85 μm , respectively.

Table 1. Three types of PhC VCSELS with different PhC designs.

	b/a	a (μm)	b (μm)	Metal Opening (μm)	Implant Aperture (μm)	Optical Aperture (μm)
PhC VCSEL-(1)	0.6	5	3	13	17	7
PhC VCSEL-(2)	0.7	3.5	2.45	9.45	13.45	4.55
PhC VCSEL-(3)	0.7	4.5	3.15	12.15	16.15	5.85

2.2. QAM-OFDM Data Transmission Analysis

For complex data format transmission, the experimental setup and block diagram of the 16-QAM OFDM encoding process were used to directly modulate the PhC VCSEL, enabling 100 m-long OM5-MMF transmission, as shown in Figure 2. The OM5-MMF with lower modal dispersion replaced the traditional OM4-MMF to achieve a higher data rate by the 400GBASE-SR16 of IEEE 802.3bs [38]. The 16-QAM OFDM data stream was encoded and decoded using a customized MATLAB program. Initially, pseudo-random bit sequence OOK data with a pattern length of $2^{15}-1$ were mapped onto the 16-QAM format with a 4×4 constellation. The 16-QAM data were uploaded serial-to-parallel onto 84 OFDM subcarriers. After the serial-to-parallel conversion, the time-domain OFDM waveform was generated by transforming the OFDM carried data using inverse fast Fourier transform with a fast Fourier transform matrix size of 512. Before digital-to-analog conversion, a cyclic prefix with a data-length ratio of 1/32 and a training symbol with a data-length ratio of 1/32 was sequentially added to the time-domain OFDM waveform to prevent inter-symbol interference and facilitate the channel response. The arbitrary waveform generator (AWG, Keysight M8196) exported the time-domain data waveform at a sample rate of 92 GSa/s. Note that the 16-QAM-OFDM subcarrier spacing is 179 MHz, determined by the formula (sampling rate/FFT size).

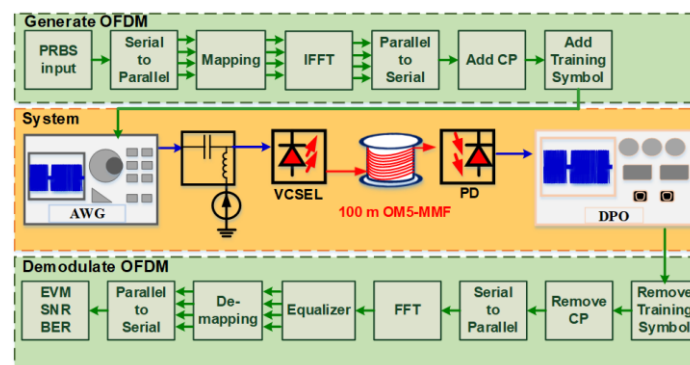


Figure 2. Block diagram of the encoding (upper) and decoding (lower) algorithms for 16-QAM OFDM transmission and the experimental setup (middle) for the directly modulating PhC VCSEL to transmit the optical 16-QAM-OFDM data stream over 100 m OM5-MMF.

The electrical 16-QAM OFDM data were then combined with the DC bias current to drive the PhC VCSEL via a bias tee (Anritsu, V250, Atsugi, Japan) with a 3 dB bandwidth of 60 GHz. This signal was fed into the VCSEL chip contact via a coplanar ground-signal-ground (GSG) probe (GGB, 40A-GSG-125-DP, Naples, FL, USA). To ensure stable VCSEL chip output encoding, the device temperature was accurately controlled using a water-cooling heat sink. For short-reach transmission in MMF, the VCSEL chip output was collected by a lensed MMF and was imported into a 100 m OM5 MMF, simulating rack-to-rack intra-data-center transmission. At the optical receiving end, the optical carrier with carried QAM-OFDM data was O-to-E converted by a high-speed photodetector (Newfocus, 1484-A50, San Jose, CA, USA), which was resampled by a digital serial analyzer (Tektronix, DPO77002SX, Beaverton, OR, USA) at a sampling rate of 200 GS/s. Finally, the received QAM-OFDM data waveform was decoded using the MATLAB program to determine its EVM, SNR, and BER performances.

3. Results

3.1. Device Characteristics of the Three PhC VCSELS

Figure 3 shows the power-current-voltage (P-I-V) responses of the PhC VCSELS. For the PhC VCSEL-(1), the threshold current can be measured as 4.2 mA with a corresponding differential quantum efficiency of 0.11. For the PhC VCSEL-(2), the threshold current of 2 mA and the quantum efficiency of 0.08 can be obtained. In previous works, the efficiency and threshold current of the PhC VCSEL were dependent on the etching depth of the PhC structure, the epitaxial structure of the VCSEL, and the relative size of the current aperture and transverse optical mode [39,40]. The etching depth of the PhC structure will affect the spectral and spatial mode-gain overlaps. To avoid the threshold current and quantum efficiency affected by the etching depth of the PhC structure, the etching depth in this work is controlled at 90–100%. In addition, the spectral mode-gain overlap is also determined by the epitaxial structure of the VCSEL. For comparison, the epitaxial structures of the PhC VCSEL for the three cases are almost the same. For the PhC VCSEL, the spatial mode-gain overlap is also determined by the relative size of the current aperture and optical mode. Therefore, the PhC structure becomes an important factor in influencing the threshold current and quantum efficiency. The effective refractive indices for the PhC-structured core ($n'_{eff,core}$) and cladding ($n'_{eff,clad}$) DBR regions are defined as $n_{eff} - \gamma \Delta n$ with n_{eff} denoting the effective refractive index of the original core and cladding region, γ ranging from 0 to 1 denoting the factor related to the etching depth of the PhC structure, and Δn denoting the decrement of the material index in the PhC-structured DBR region [40,41]. By defining the confinement factor as $\Gamma' = \{1 + \lambda^2 / [2\pi^2 d^2 (n'^2_{eff,core} - n'^2_{eff,clad})]\}^{-1}$ with λ and d indicating the lasing wavelength and the core diameter of the PhC-structured VCSEL [42], the differential quantum efficiency (η'_d) is modified as [43–45]

$$\eta'_d = \eta_i \left(1 - \frac{\alpha_i}{g't_h}\right) = \eta_i \left(1 - \frac{\alpha_i}{\frac{1}{\Gamma'} \left[\alpha_i + \frac{1}{2L} \ln\left(\frac{1}{R'_1 R'_2}\right)\right]}\right) = \frac{hc}{q\lambda} \frac{dP}{dI} \tag{1}$$

where $g't_h$, α_i , L , R'_i , h , c , q , P , and I , denote the threshold gain, the net internal optical loss, the cavity length, the mirror reflectivity, the Planck constant, the speed of light, the electron charge, the optical power, and the bias current respectively. Owing to the modification of the effective refractive indices in the PhC-structured core and cladding regions, both the confinement factor and gain threshold were deviated to change the differential quantum efficiency. The PhC VCSEL-(2) shows a reduced $n'_{eff,clad}$ to increase the confinement factor. From Equation (1), the increased confinement factor suppresses the threshold gain to decrease the threshold current. Although the enhanced confinement factor achieved by incorporating the PhC structure in the cladding promotes the generation of more coherent photons in the VCSEL cavity, the effective output photon numbers remain limited to reduce the η'_d of the PhC VCSEL-(2). When an additional 1-period PhC pattern in the core region reduces the $n'_{eff,core}$ to reduce the confinement factor, the threshold current of the PhC

VCSEL-(3) slightly enlarges from 2 to 2.9 mA. However, the differential quantum efficiency further decreases from 0.08 to 0.04, as obtained from the first-order derivative of the power-to-current response of the PhC-structured VCSELs. For the PhC VCSEL-(3), the effective refractive index within the core region is reduced because the PhC pattern results in a weaker confinement factor than PhC VCSEL-(2). This weak confinement factor increases the threshold gain to enlarge the threshold current and differential quantum efficiency. However, the PhC patterns in the core region significantly suppress the emission aperture to limit the output power and mode number. Therefore, the differential quantum efficiency of the PhC VCSEL-(3) still shows degradation. Generally, the PhC structure influences the resistance of the VCSEL to cause signal reflection during modulation. For the V-I response, the PhC VCSEL-(1) shows a differential resistance of 32Ω at a bias current of 10 mA, resulting in a corresponding reflection coefficient of 0.22 and a return loss of -13.1 dB . For the PhC VCSEL-(2), the PhC structure damages the top DBR mirror layer to increase the series resistance. Hence, the differential resistance of the PhC VCSEL-(2) enlarges to 36Ω with a reflection coefficient of 0.16 and a return loss of -15.7 dB . When the PhC pattern is incorporated into the core region, the series resistance for the PhC VCSEL-(3) is further enlarged to enhance its differential resistance of 39Ω . This change also provides an improved reflection coefficient of 0.12 and a return loss of -18.1 dB . For the signal reflection, the device resistance approaches the characteristic resistance of 50Ω to allow for better modulation depth. Ideally, the PhC VCSEL-(3) would exhibit the best modulation depth during the modulation.

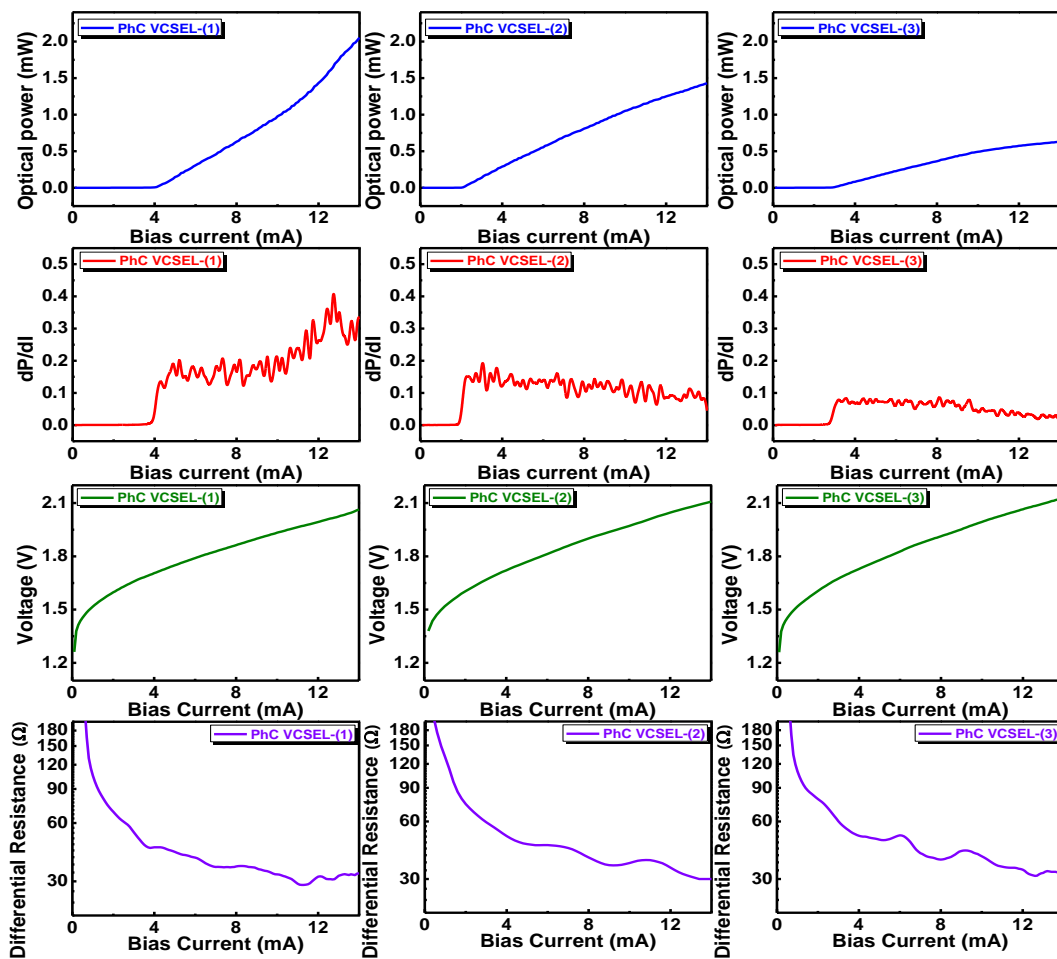


Figure 3. P-I, dP/dI, V-I, and dV/dI responses of three different PhC VCSELs.

To examine the effect of the core/cladding PhC structure on the lasing mode number of the multi-mode VCSEL, the optical spectra of various PhC VCSELs under different I_{bias} conditions are shown and compared in Figure 4. The PhC VCSEL-(2) exhibits some specific spectral features compared to PhC VCSEL-(1) due to its additional PhC structure in the cladding. For the original VCSEL, its central wavelength (λ_c) is located at 858.6 nm, and its lasing mode number (N_{mode}) increases from 1 to 3 as the bias current increases from 5 mA to 13 mA to provide enough gain for high-order lasing modes. With the insertion of 2-period PhC patterns in the cladding region, the PhC VCSEL blue-shifts the lasing wavelength and lowers the threshold current. This results in a λ_c and N_{mode} for the PhC VCSEL-(2) with only one-mode lasing at 857.7 nm under a bias current of 3 mA. The λ_c gradually red-shifts to 859.7 nm, and the N_{mode} increases to 7 as the bias current enlarges to 13 mA. The increased N_{mode} raising the bias current to 13 mA is due to the sufficient gain of the PhC VCSEL-(2), which can excite high-order modes at the core boundary. Under high-bias conditions, the PhC VCSEL-(2) exhibits more modes than the PhC VCSEL-(1) since its confinement factor is improved to facilitate higher-order modes lasing in the cavity with a larger numerical aperture and gain. To understand the influence of introducing the PhC structure into the core layer, the PhC VCSEL-(3) is compared to the PhC VCSEL-(2). For the PhC VCSEL-(3), its core PhC reduces the emission aperture by enlarging the cavity mirror loss in the central region to prevent high-order-mode lasing. However, the threshold current of the PhC VCSEL-(3) enlarges. Hence, the PhC VCSEL-(3) shows a red-shifted lasing spectrum with only a single-transverse mode at a bias current between 3 and 13 mA. This shows the unique effect of the core/cladding PhC on strictly controlling the transverse mode number of the VCSEL.

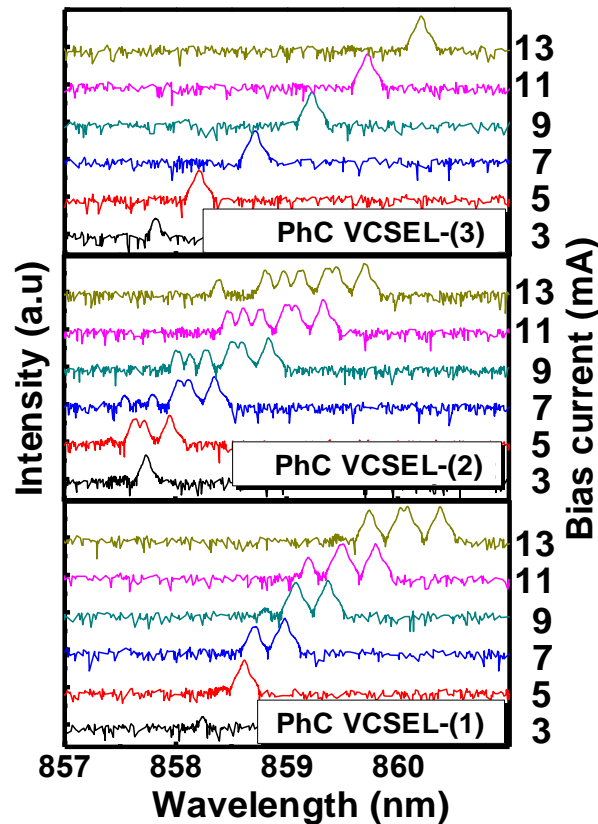


Figure 4. Corresponding optical spectrum of the different PhC VCSEL designs.

To discuss the spectral linewidth of multi-mode VCSELs, the transverse-mode distribution of the PhC VCSEL can be quantified by introducing the root-mean-square spectral linewidth ($\Delta\lambda_{RMS}$) as defined by the IEEE P802.3bs standard as [46,47]

$$\Delta\lambda_{RMS} = \sqrt{\left[\frac{\sum_{i=1}^n P_i \left(\lambda_i - \frac{\sum_{i=1}^n P_i \lambda_i}{\sum_{i=1}^n P_i} \right)^2}{\sum_{i=1}^n P_i} \right]} \quad (2)$$

where P_i and λ_i denote the peak power and wavelength of the i_{th} modes in the optical spectrum with power extinction of <20 dB compared to the central peak, respectively. From Figure 4, the PhC VCSEL-(1) and PhC VCSEL-(2) display 3 and 7 transverse modes at a bias current of 13 mA with their corresponding $\Delta\lambda_{RMS}$ of 0.22 and 0.28, respectively. In contrast, the $\Delta\lambda_{RMS}$ of the PhC VCSEL-(3) is determined to be 0 nm due to its single-transverse mode output.

Although all PhC VCSELs meet the IEEE P802.3ae standard ($\Delta\lambda_{RMS} < 0.45$ nm) [48], the aforementioned PhC VCSEL with $\Delta\lambda_{RMS}$ of 0 would benefit from minimal suffer less modal dispersion during transmission in the MMF. Due to the single-transverse mode output with $\Delta\lambda_{RMS}$ of 0, the PhC VCSEL-(3) emerges as the most promising candidate for transmitting data over MMF while minimizing modal dispersion.

To optimize the signal-to-noise extinction without compromising the allowable bandwidth of the PhC VCSEL, the RIN is characterized to identify the optimal PhC structure design for the VCSELs. During direct modulation, the RIN spectrum of the PhC VCSEL exhibits a high-frequency peak due to its relaxation oscillation nature. It enlarges the intensity noise level in the signal spectrum to impact the SNR performance of the carried QAM-OFDM data. The RIN responses of the PhC VCSEL are also influenced by different PhC structures, as compared in Figure 5. The RIN spectrum is recorded using a lightwave signal analyzer (HP, 71300C). For the PhC VCSEL-(1), its RIN peak energy and position at a bias current of 5 mA are -120 dBc/Hz and 3.2 GHz, respectively. These values can be slightly reduced by 1 dBc/Hz and up-shifted by 1.8 GHz when the bias current increases to 14 mA. Generally, the relaxation oscillation frequency (f_r) of a VCSEL is defined as [47]:

$$f_r = \frac{1}{2\pi} \sqrt{\frac{\Gamma V_g G \eta_i (I - I_{th})}{q V_{opt}}} \quad (3)$$

with the RIN spectral shape as a Lorentzian function of f_r as expressed by [47]:

$$RIN(f) \propto \frac{f^2 + (\gamma/2\pi)^2}{(f_r^2 - f^2)^2 + f^2(\gamma/2\pi)^2} \quad (4)$$

where γ denotes the damping coefficient. Equation (3) interprets that the RIN peak is inversely proportional to f_r , and a higher bias current results in a higher f_r and a lower RIN peak intensity. By implementing a bi-layer cladding PhC confinement in the PhC VCSEL-(2), the RIN peak energy and position are significantly reduced to -135 dBc/Hz and up-shifted to 5 GHz at a 5-mA bias current, respectively. This improvement over PhC VCSEL-(1) is primarily due to the enhanced cladding confinement, which betters the lasing conditions by reducing the bias current under the PhC control in the cladding region. According to Equation (2), increasing the bias current or lowering the threshold current can raise the f_r to suppress and up-shift the RIN peak. When the bias current of PhC VCSEL-(2) is raised to 14 mA, the RIN peak further shifts up to 17.5 GHz with a peak energy of -126 dBc/Hz, while its average noise background notably decreases to -143 dBc/Hz. The high-order modes of the PhC VCSEL-(2) are excited at highly biased conditions to induce additional RIN that superimposes with the RIN spectrum from the fundamental mode. Introducing a one-period PhC pattern into the core to form the PhC VCSEL-(3) increases the threshold current conversely, resulting in the RIN peak down-shifting back to

4.7 GHz with a peak energy of -126 dBc/Hz at a bias current of 5 mA. The RIN peak fully merges into the noise background when the bias current is further increased to 14 mA. PhC VCSEL-(3) is a single-mode laser to suppress additional noise in the RIN spectrum even at high-bias operation. Except for these RIN peaks, the overall RIN noise level can be as low as -140 dBc/Hz.

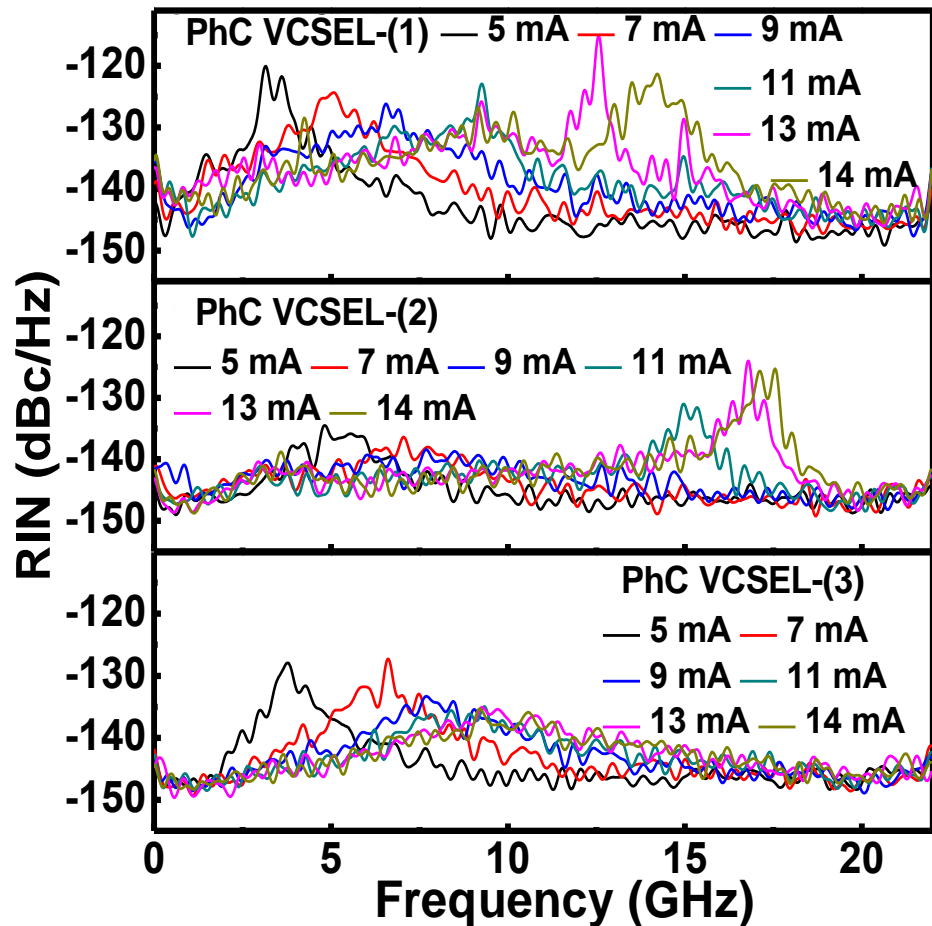


Figure 5. RIN responses of PhC VCSELs with different structures and bias currents.

3.2. Transmission of Pre-Compensated 16-QAM-OFDM and Bit-Loaded QAM-OFDM Data

A distortion pre-compensation technique was employed to further increase the allowable bandwidth of the 16-QAM-OFDM data and to maximize the transmission capacity. This technique adjusts the transmission power of each OFDM subcarrier to counteract the degraded response caused by the PhC VCSEL and the transmission link [21]. Pre-compensated QAM-OFDM data sacrifice their low-frequency OFDM subcarrier power to compensate for the high-frequency OFDM power for SNR improvement [49]. Figure 6a illustrates the constellation plots, subcarrier SNR, and decoded BER of pre-compensated 16-QAM-OFDM data in the BtB transmission of three PhC VCSELs. The PhC VCSEL-(1) can only deliver the QAM-OFDM data at 12 GHz without distortion compensation. Expanding the bandwidth to 13 GHz with a pre-compensation slope of $+0.1$ dB/GHz only improves its EVM, SNR, and BER to 18.2%, 14.8 dB, and 5.2×10^{-3} , respectively. Further increasing the pre-leveling slope inversely affects the BER of OFDM data as the PhC VCSEL-(1) output power is insufficient for OFDM subcarrier power rearrangement.

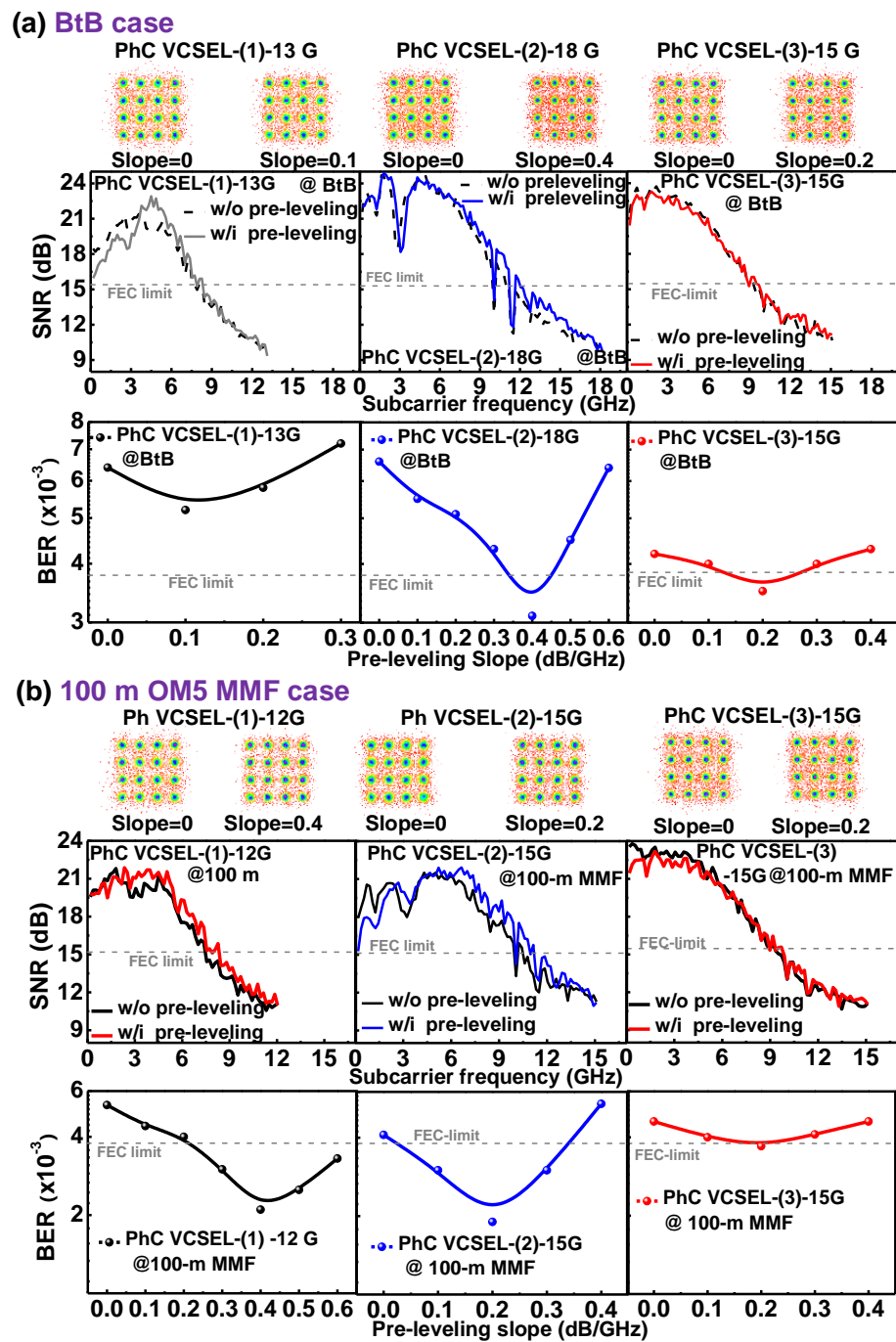


Figure 6. Constellation plots, SNR, and BER of the 16-QAM-OFDM data carried by the three PhC VCSEL chips under the optimized bandwidth operation with and without distortion pre-compensation in the BtB and 100 m OM5-MMF cases.

Using PhC VCSEL-(2) to carry the QAM-OFDM data allows for a significant increase in the effective bandwidth to 18 GHz with a pre-compensating slope of 0.4 dB/GHz. This results in an EVM of 16.9%, an SNR of 15.4 dB, and a BER of 3.1×10^{-3} at 72 Gbit/s. When continually raising the pre-leveling slope to 0.6 dB/GHz, the EVM, BER, and SNR of the OFDM data reduce to 18.8%, 14.5 dB, and 6.6×10^{-3} , respectively. In comparison, the acceptable modulation bandwidth of the PhC VCSEL-(3)-carried OFDM data can be optimized to 15 GHz with a pre-compensation slope of 0.2 dB/GHz for providing an EVM of 17.2%, an SNR of 15.1 dB, and a BER of 3.5×10^{-3} at 60 Gbit/s. A larger 0.4 dB/GHz slope degrades the EVM, SNR, and BER of the OFDM data to 17.7%, 15 dB, and

4.3×10^{-3} , respectively. Comparing PhC VCSEL-(2) and PhC VCSEL-(3) shows that a smaller output power device can limit the pre-compensation performance. Hence, the optimization slope for the PhC VCSEL-(3)-carried OFDM data becomes narrower than that for the PhC VCSEL-(2)-carried data. After propagating the 100 m OM5 MMF, the effect of the distortion pre-leveling on the improvements in EVM, SNR, and BER performance for the 16-QAM OFDM data carried by the three PhC VCSELs are compared in Figure 6b. As expected, the pre-compensation can enlarge the allowable bandwidth of the OFDM data carried by PhC VCSEL-(1) from 11 to 12 GHz after 100 m OM5-MMF transmission, which optimizes the constellation plot with a slope of 0.4 dB/GHz to provide an EVM suppressed from 18.2% (slope = 0) to 16.1%. Figure 6b illustrates that the SNR and BER responses can improve from 14.8 to 15.8 dB and 5.3×10^{-3} to 2.1×10^{-3} , respectively. In contrast, the PhC VCSEL-(2) broadens its QAM-OFDM bandwidth from 14 to 15 GHz after 100 m OM5-MMF transmission by pre-compensating its subcarrier amplitude at a slope of 0.2 dB/GHz, revealing an optimized EVM of 15.9%, an optimized SNR of 16 dB, and an optimized BER of 1.9×10^{-3} . The OFDM data carried by the PhC VCSEL-(3) exhibit the same bandwidth of 15 GHz after pre-compensation at a slope of 0.2 dB/GHz, with an EVM of 17.3%, an SNR of 15.2 dB, and a BER of 3.7×10^{-3} . The OFDM transmission performance for the PhC VCSEL-(2) with a higher power is better than that for the PhC VCSEL-(3), although the former device has more transverse modes. Compared with comparable output power, the OFDM data carried by the PhC VCSEL-(3) provides even better performance after 100 m OM5-MMF transmission with pre-compensation, as its single-transverse mode feature inherently prevents distortion from modal dispersion.

To further improve the data rate for the PhC VCSEL, the bit-loading technique is used to allocate suitable QAM levels for OFDM subcarriers at different frequency regions [50–52]. Figure 7a shows the distributions of suitable QAM-level loading for different OFDM subcarriers carried by three PhC VCSELs in the BtB case. From the subcarrier frequency-dependent SNR responses for different PhC VCSELs shown in Figure 7a, the PhC VCSEL-(1) can simultaneously transmit 32-QAM, 8-QAM, and 4-QAM OFDM data within the 14.3 GHz encoding bandwidth. The detailed transmission results are listed as Table 2. The respective data rates of the 32, 8, and 4 QAM-OFDM data transmitted by PhC VCSEL-(1) are 48, 9, and 3.2 Gbit/s, to provide a total data rate of 60.7 Gbit/s. Using the PhC VCSEL-(2), the 32/8/4 QAM-OFDM data stream can provide the available bandwidth of 13.3/2.5/5.5 GHz to successfully improve the overall data rate up to 85 Gbit/s in the BtB case. When transferring the optical carrier to the PhC VCSEL-(3), the bit-loading allows 16 and 4 QAM-OFDM for direct encoding within bandwidths of 14 and 4.5 GHz, respectively, to provide a data rate of 65 Gbit/s in total. Compared with broadband and bit-loading QAM-OFDM techniques, the encodable data rates for the three PhC VCSELs under BtB transmission are significantly improved from 48/64/56 to 60.7/85/65 Gbit/s. The PhC VCSEL-(2) is realized as the best transmitter candidate among all the proposed PhC VCSEL designs to possess the widest 3 dB frequency bandwidth and the lowest roll-off effect to enable the largest transmission capacity. Finally, the bit-loading QAM-OFDM improves the 100 m MMF transmission performance. Figure 7b shows the QAM-level distribution profile versus the subcarrier number for different PhC VCSELs, while Figure 7b shows the subcarrier SNR responses. After 100 m MMF transmission, the PhC VCSEL-(1) delivers the bit-loaded 32/8/4 QAM-OFDM data to decrease the bandwidths of 9.3/3.2/1.2 GHz. When replacing the optical carrier with the PhC VCSEL-(2) through 100 m MMF, the PhC VCSEL-(2) can deliver the bit-loaded QAM-OFDM data stream with a data rate of 81.2 Gbit/s. Using the PhC VCSEL-(3) can only bit-load 16 and 4 QAM-OFDM data with a bandwidth of 18.6 GHz to provide a total data rate of 64.6 Gbit/s.

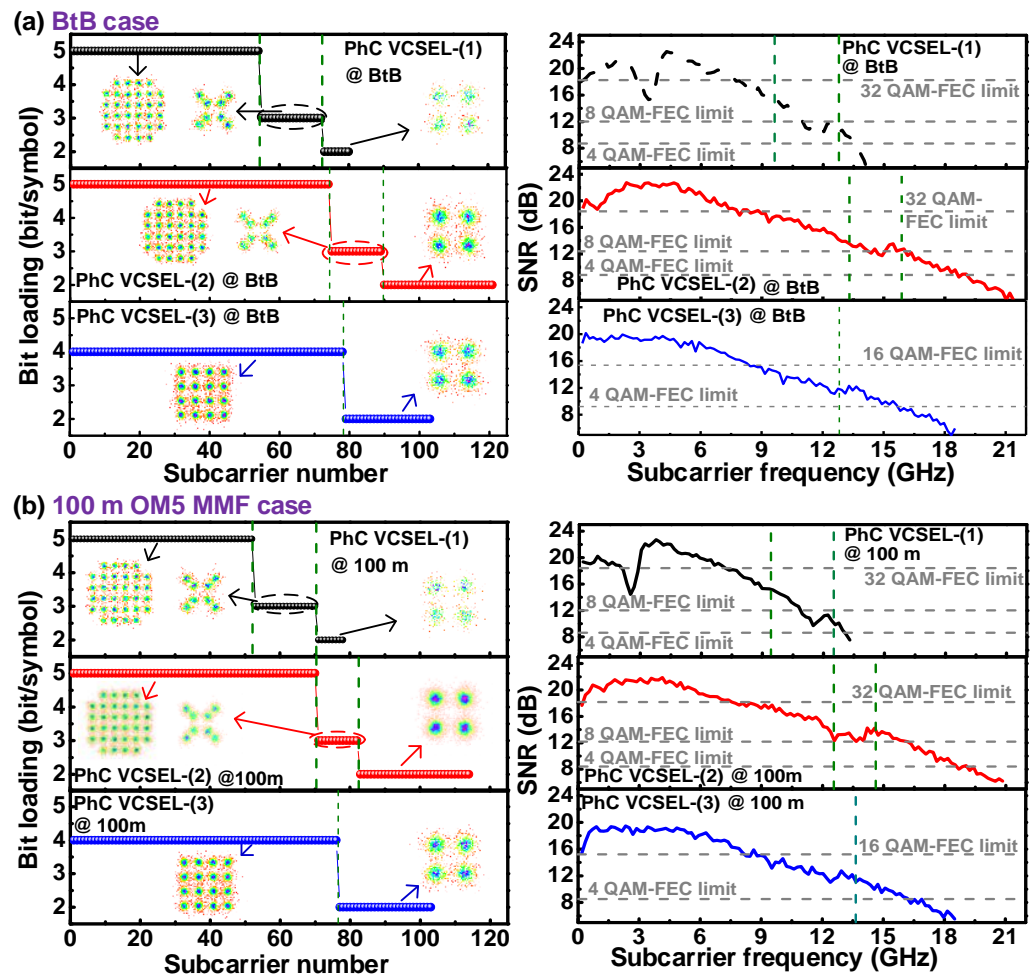


Figure 7. (a) Optimal bit-loading distribution and (b) SNR versus subcarrier frequency for different PhC VCSELs with the bit-loading technique in the (a) BtB and 100 m OM5-MMF cases.

To further optimize the transmission capacity, the tilting angle is adjusted from 7° to 0° to improve the collection of the output power. Furthermore, the data synthesizer is upgraded to an AWG (Keysight, M8194, Santa Rosa, CA, USA) with a 50 GHz analog bandwidth and a 120-GSa/s sampling rate to minimize data distortion. Figure 8 shows the QAM-level distribution profile and the subcarrier-frequency-dependent SNR of the bit-loaded QAM-OFDM data transmitted by the PhC VCSEL-(2) in both BtB and 100 m OM5-MMF cases after optimizing the tilting angle and increasing the sampling rate. Table 3 exhibits the related performance parameters. For the PhC VCSEL-(2), the 32/16/8/4 QAM-OFDM and BPSK data streams can support the available bandwidth of 8.7/6.6/4.5/5.3/4.9 GHz to successfully improve the overall data rate up to 98.9 Gbit/s in the BtB case. After 100 m OM5-MMF transmission to induce a larger propagation loss, the PhC VCSEL-(2) only delivers the bit-loaded 32/16/8/4 QAM-OFDM and BPSK data to decrease the bandwidths of 5.9/4.7/12.7/2.1/3.8 GHz. Notably, PhC VCSEL-(2) can deliver the bit-loaded QAM-OFDM data stream with the highest data rate reaching 95.3 Gbit/s. These results highlight the trade-off design of core/cladding PhC structures for MM VCSELs in achieving broadband or bit-loading QAM-OFDM data transmission. Among the three selected designs, the experimental results show that PhC VCSEL-(2) with the highest lasing power provides the broadest bandwidth and the highest data rate for future applications in transmitting high-spectral-density QAM-OFDM data formats in data centers.

Table 2. The detailed performance parameters of the bit-load QAM-OFDM data carried by the three different PhC VCSELs in the BtB and 100 m OM5-MMF cases.

Btb Case			
PhC VCSEL-(1)			
QAM level	32-QAM	8-QAM	4-QAM
Bandwidth	9.7 GHz	3 GHz	1.6 GHz
EVM	11.7%	24.3%	34.7%
SNR	18.6 dB	12.3 dB	9.2 dB
BER	2.8×10^{-3}	3.1×10^{-3}	1.9×10^{-3}
Total Data Rate	60.7 Gbit/s		
PC VCSEL(2)			
QAM level	32-QAM	8-QAM	4-QAM
Bandwidth	13.3 GHz	2.5 GHz	5.5 GHz
EVM	12%	24%	37.1%
SNR	18.4 dB	12.4 dB	8.6 dB
BER	3.1×10^{-3}	2.6×10^{-3}	3.4×10^{-3}
Total Data Rate	85 Gbit/s		
PhC VCSEL-(3)			
QAM level	16-QAM	4-QAM	
Bandwidth	14 GHz	4.5 GHz	
EVM	17.2%	37.2%	
SNR	15.3 dB	8.6 dB	
BER	3.5×10^{-3}	3.5×10^{-3}	
Total Data Rate	65 Gbit/s		
100 m OM5-MMF case			
PhC VCSEL-(1)			
QAM level	32-QAM	8-QAM	4-QAM
Bandwidth	9.3 GHz	3.2 GHz	1.2 GHz
EVM	12%	24.5%	36.3%
SNR	18.5 dB	12.2 dB	8.8 dB
BER	2.9×10^{-3}	3.2×10^{-3}	2.8×10^{-3}
Total Data Rate	58.5 Gbit/s		
PhC VCSEL-(2)			
QAM level	32-QAM	8-QAM	4-QAM
Bandwidth	12.6 GHz	2.2 GHz	5.8 GHz
EVM	12.3%	23.4%	32.7%
SNR	18.2 dB	12.6 dB	9.7 dB
BER	3.8×10^{-3}	2.2×10^{-3}	1.6×10^{-3}
Total Data Rate	81.2 Gbit/s		
PhC VCSEL-(3)			
QAM level	16-QAM	4-QAM	
Bandwidth	13.7 GHz	4.9 GHz	
EVM	17.2%	36.7%	
SNR	15.3 dB	8.7 dB	
BER	3.6×10^{-3}	3.2×10^{-3}	
Total Data Rate	64.6 Gbit/s		

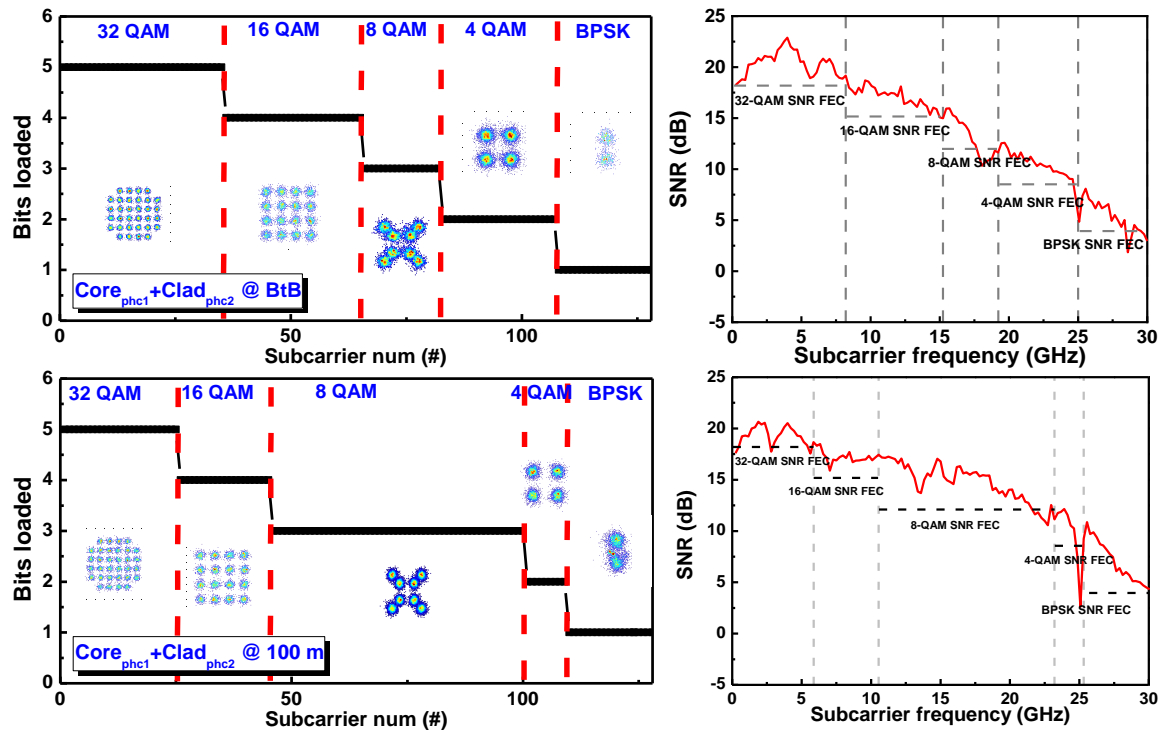


Figure 8. QAM-level distribution profile and the subcarrier-frequency-dependent SNR of the bit-loaded QAM OFDM data delivered by PhC VCSEL-(2) in the BtB and 100 m OM5-MMF cases after the optimization of the tilting angle and the improvement of the sampling rate.

Table 3. The detailed performance parameters of the bit-load QAM-OFDM data carried by the PhC VCSEL-(2) in the BtB and 100 m OM5-MMF cases after the optimization of the tilting angle and the improvement of the sampling rate.

BtB case					
QAM level	32-QAM	16-QAM	8-QAM	4-QAM	BPSK
Bandwidth	8.7 GHz	6.6 GHz	4.5 GHz	5.3 GHz	4.9 GHz
SNR	19.6 dB	16.4 dB	12.3 dB	9.2 dB	4.6 dB
BER	9.3×10^{-4}	1.2×10^{-3}	3.1×10^{-3}	2.1×10^{-3}	1.9×10^{-3}
Total Data Rate	98.9 Gbit/s				
100 m OM5-MMF case					
QAM level	32-QAM	16-QAM	8-QAM	4-QAM	BPSK
Bandwidth	5.9 GHz	4.7 GHz	12.7 GHz	2.1 GHz	4.7 GHz
SNR	18.8 dB	16.7 dB	14 dB	10 dB	6.7 dB
BER	2.2×10^{-3}	8.4×10^{-4}	4.5×10^{-4}	8.1×10^{-4}	1.2×10^{-4}
Total Data Rate	95.3 Gbit/s				

4. Conclusions

We have compared the pre-compensated and bit-loaded QAM-OFDM data encoding and transmission performance for three 850 nm VCSELs with different PhC designs. Three PhC VCSELs were created using proton-bombardment isolation to define the emission aperture and implement PhC structures in the core/cladding region. PhC VCSEL-(1) exhibits a threshold current of 4.2 mA and an $\Delta\lambda_{RMS}$ of 0.22 nm to provide a modulation bandwidth of 14.3 GHz with a background RIN of -126 dBc/Hz at an optimized bias current of 14 mA. Hence, PhC VCSEL-(1) can only carry 16-QAM-OFDM data through BtB and 100 m MMF transmission with respective allowable bit rates of 48 Gbit/s and

44 Gbit/s. Employing the waveform pre-compensation slightly extends the OFDM data in 100 m OM5-MMF transmission to 48 Gbit/s with the corresponding EVM/SNR/BER of 16.1%/15.8 dB/ 2.1×10^{-3} , respectively. When performing bit-loading, the data rates in the BtB and 100 m OM5-MMF cases further improve to 60.7/58.5 Gbit/s within the modulation bandwidths of 14.3/13.7 GHz, respectively. PhC VCSEL-(2) with PhC confined cladding can provide the smallest bias current of 2 mA and the highest 3 dB bandwidth of 15 GHz at the same bias current of 14 mA to exhibit a multi-mode output with $\Delta\lambda_{RMS}$ of 0.28 nm and background RIN of -143 dBc/Hz. The allowable bandwidth for 16-QAM-OFDM data can be optimized at 16 GHz. Additionally, the data rate is slightly degraded to 14(56) GHz(Gbit/s) even with modal dispersion after 100 m OM5-MMF transmission. The pre-compensation with a power-to-frequency slope of 0.2 dB/GHz resumes the allowable bandwidth after 100 m OM5-MMF back to 15 GHz for 60-Gbit/s QAM-OFDM with EVM/SNR/BER of 15.9%/16 dB/ 1.9×10^{-3} , respectively. The bit-loading further promotes the data rate of OFDM data up to 85/81.2 Gbit/s within the modulation bandwidths of 21.3/21 GHz before and after 100 m OM5-MMF transmissions. Using the PhC patterns in both core/cladding regions for PhC VCSEL-(3), the single-mode output achieves the $\Delta\lambda_{RMS}$ of 0 nm, a threshold current of 2.9 mA, 3 dB bandwidth of 12.9 GHz, and a background RIN of -140 dBc/Hz. Although the modal dispersion during OM5-MMF transmission can be suppressed, its effective throughput power is also reduced to -2 dBm at the same bias current of 14 mA. The allowable bandwidths of the 16-QAM OFDM data carried by the PhC VCSEL-(3) before and after 100 m OM5-MMF transmissions remain the same as 14 GHz with an effective data rate of 56 Gbit/s. As transmitting power attenuation and chromatic dispersion still affect the carried OFDM data, the 16-QAM-OFDM data pre-compensating with a slope of 0.2 dB/GHz enables a 15 GHz bandwidth for 100 m OM5-MMF transmission with an EVM of 17.3%, an SNR of 15.2 dB, and a BER of 3.7×10^{-3} . Bit-loaded QAM-OFDM-based BtB/100 m-OM5-MMF transmission improves the data rate to 65/64.6 Gbit/s with 18.5/18.6 bandwidths, respectively. Finally, optimizing the tilting angle from 7° to 0° to increase the coupling power and improving the sampling rate of the transmitted data to avoid data distortion can enhance the allowable data rates of the bit-loaded QAM-OFDM data carried by the PhC VCSEL-(2) to 98.9 Gbit/s and 95.3 Gbit/s in the BtB and 100 m OM5-MMF cases, respectively. The results suggest that the core/cladding PhC structure trade-off significantly impacts the allowable bandwidth (data rate) of the MM VCSEL. Cladding the PhC structure improves the optical confinement and SNR, while the core PhC structure assists single-mode lasing with slightly reduced power. Cladding PhC confinement optimizes the MM VCSEL for improving direct encoding and dispersion-suppressed data transmission performance in the data-center link.

Author Contributions: Conceptualization, G.-R.L. and K.D.C.; methodology, K.D.C.; validation, Y.-H.L. and G.-R.L.; formal analysis, Y.-H.L., C.-H.C., C.-T.T. and W.-L.W.; data curation, Y.-H.L.; writing—original draft preparation, Y.-H.L. and C.-H.C.; writing—review and editing, C.-H.C., G.-R.L. and K.D.C.; supervision, G.-R.L. and K.D.C.; project administration, G.-R.L. and K.D.C.; funding acquisition, G.-R.L. All authors have read and agreed to the published version of the manuscript.

Funding: This work was supported by the National Science and Technology Council, Taiwan, under grants MOST 109-2221-E-002-184-MY3, MOST 110-2221-E-002-100-MY3, MOST 111-2124-M-A49-004-, NSTC 111-2119-M-002-009-, NSTC 111-2622-E-002-035-, NSTC 111-3114-E-002-001-, NSTC 111-2221-E-002-143-MY3, NSTC 111-2224-E-A49-001-, and NSTC 112-2119-M-002-013-.

Institutional Review Board Statement: Not applicable.

Informed Consent Statement: Not applicable.

Data Availability Statement: The data presented in this study are available upon request from the corresponding author.

Conflicts of Interest: The authors declare no conflict of interest.

References

1. Westbergh, P.; Gustavsson, J.; Haglund, A.; Sunnerud, H.; Larsson, A. Large aperture 850 nm VCSELs operating at bit rates up to 25 Gbit/s. *Electron. Lett.* **2008**, *44*, 907–908. [\[CrossRef\]](#)
2. Tatum, J.A.; Gazula, D.; Graham, L.A.; Guenter, J.K.; Johnson, R.H.; King, J.; Kocot, C.; Landry, G.D.; Lyubomirsky, I.; MacInnes, A.N.; et al. VCSEL-Based Interconnects for Current and Future Data Centers. *J. Light. Technol.* **2015**, *33*, 727–732. [\[CrossRef\]](#)
3. Tan, F.; Wu, M.-K.; Liu, M.; Feng, M.; Holonyak, N. 850 nm Oxide-VCSEL With Low Relative Intensity Noise and 40 Gb/s Error Free Data Transmission. *IEEE Photonics Technol. Lett.* **2014**, *26*, 289–292. [\[CrossRef\]](#)
4. Huang, C.-Y.; Wang, H.-Y.; Wu, C.-H.; Cheng, C.-H.; Tsai, C.-T.; Wu, C.-H.; Feng, M.; Lin, G.-R. Comparison of high-speed PAM4 and QAM-OFDM data transmission using single-mode VCSEL in OM5 and OM4 MMF links. *IEEE J. Sel. Top. Quantum Electron.* **2020**, *26*, 1500210. [\[CrossRef\]](#)
5. Chi, K.-L.; Shi, Y.-X.; Chen, X.-N.; Chen, J.; Yang, Y.-J.; Kropp, J.-R.; Ledentsov, N., Jr.; Agustin, M.; Ledentsov, N.N.; Stepniak, G.; et al. Single-mode 850-nm VCSELs for 54-Gb/s ON-OFF keying transmission over 1-km multi-mode fiber. *IEEE Photonics Technol. Lett.* **2016**, *28*, 1367–1370. [\[CrossRef\]](#)
6. Blokhin, S.A.; Lott, J.A.; Mutig, A.; Fiol, G.; Ledentsov, N.N.; Maximov, M.V.; Nadtochiy, A.M.; Shchukin, V.A.; Bimberg, D. Oxide-confined 850 nm VCSELs operating at bit rates up to 40 Gbit/s. *Electron. Lett.* **2009**, *45*, 501–503. [\[CrossRef\]](#)
7. Chen, C.; Tian, Z.; Choquette, K.D.; Plant, D.V. 25-Gb/s direct modulation of implant confined holey vertical-cavity surface-emitting lasers. *IEEE Photonics Technol. Lett.* **2010**, *22*, 465–467. [\[CrossRef\]](#)
8. Chang, Y.-C.; Wang, C.; Johansson, L.; Coldren, L. High-efficiency, high-speed VCSELs with deep oxidation layers. *Electron. Lett.* **2006**, *42*, 1281–1283. [\[CrossRef\]](#)
9. Zhu, B.; Taunay, T.F.; Yan, M.F.; Fishteyn, M.; Oulundsen, G.; Vaidya, D. 70-Gb/s multicore multimode fiber transmissions for optical data links. *IEEE Photonics Technol. Lett.* **2010**, *22*, 1647–1649. [\[CrossRef\]](#)
10. Zhang, Q.; Jiang, Y.; Zhou, H.; Deng, C.; Duan, S.; Wang, Z.; Li, Y.; Song, Y.; Chen, J.; Zhang, J.; et al. 137 Gb/s PAM-4 Transmissions at 850 nm over 40 cm Optical Backplane with 25 G Devices with Improved Neural Network-Based Equalization. *Appl. Sci.* **2019**, *9*, 5095. [\[CrossRef\]](#)
11. Ou, Y.; Gustavsson, J.S.; Westbergh, P.; Haglund, A.; Larsson, A.; Joel, A. Impedance Characteristics and Parasitic Speed Limitations of High-Speed 850-nm VCSELs. *IEEE Photonics Technol. Lett.* **2009**, *21*, 1840–1842. [\[CrossRef\]](#)
12. Shi, J.W.; Wei, Z.R.; Chi, K.L.; Jiang, J.W.; Wun, J.M.; Lu, I.C.; Chen, J.; Yang, Y.-J. Single-mode, high-speed, and high-power vertical-cavity surface-emitting lasers at 850 nm for short to medium reach (2 km) optical interconnects. *J. Light. Technol.* **2013**, *31*, 4037–4044. [\[CrossRef\]](#)
13. Kao, H.-Y.; Cheng, W.-H.; Wu, C.-H.; Lin, G.-R.; Tsai, C.-T.; Chi, Y.-C.; Peng, C.-Y.; Leong, S.-F.; Wang, H.-Y.; Cheng, C.-H.; et al. Long-Term Thermal Stability of Single-Mode VCSEL Under 96-Gbit/s OFDM Transmission. *IEEE J. Sel. Top. Quantum Electron.* **2019**, *25*, 1500609. [\[CrossRef\]](#)
14. Huang, C.-Y.; Tsai, C.-T.; Weng, J.-H.; Cheng, C.-H.; Wang, H.-Y.; Wu, C.-H.; Feng, M.; Lin, G.-R. Temperature and Noise Dependence of Tri-Mode VCSEL Carried 120-Gbit/s QAM-OFDM Data in Back-to-Back and OM5-MMF Links. *J. Light. Technol.* **2020**, *38*, 6746–6758. [\[CrossRef\]](#)
15. Lu, I.-C.; Wei, C.-C.; Chen, H.-Y.; Chen, K.-Z.; Huang, C.-H.; Chi, K.-L.; Shi, J.-W.; Lai, F.-I.; Hsieh, D.-H.; Kuo, H.-C.; et al. Very high bit-rate distance product using high-power single-mode 850-nm VCSEL with discrete multitone modulation formats through OM4 multimode fiber. *IEEE J. Sel. Top. Quantum Electron.* **2015**, *21*, 1701009. [\[CrossRef\]](#)
16. Hsueh, T.-H.; Kuo, H.-C.; Lai, F.-I.; Lai, L.-H.; Wang, S.-C. High-speed characteristics of large-area single-transverse-mode vertical-cavity surface-emitting lasers. *Electron. Lett.* **2003**, *39*, 1519–1521. [\[CrossRef\]](#)
17. Tan, M.P.; Fryslie, S.T.M.; Lott, J.A.; Ledentsov, N.N.; Bimberg, D.; Choquette, K.D. Error-Free Transmission Over 1-km OM4 Multimode Fiber at 25 Gb/s Using a Single Mode Photonic Crystal Vertical-Cavity Surface-Emitting Laser. *IEEE Photonics Technol. Lett.* **2013**, *25*, 1823–1825. [\[CrossRef\]](#)
18. Guo, X.; Dong, J.; He, X.; Hu, S.; He, Y.; Lv, B.; Li, C. Heat dissipation effect on modulation bandwidth of high-speed 850-nm VCSELs. *J. Appl. Phys.* **2017**, *121*, 133105. [\[CrossRef\]](#)
19. Tsai, C.-L.; Lee, F.-M.; Cheng, F.-Y.; Wu, M.-C.; Ko, S.-C.; Wang, H.-L.; Ho, W.-J. Silicon oxide-planarized single-mode 850-nm VCSELs with TO package for 10 Gb/s data transmission. *IEEE Electron Device Lett.* **2005**, *26*, 304–307. [\[CrossRef\]](#)
20. Lin, G.-R.; Cheng, C.-H.; Kuo, H.-C.; Lee, S.-Y.; Chen, X.; Wang, C.-H.; Li, M.-J.; Huang, Y.-M.; Huang, W.-T.; Yang, D. Nearly 70 Gbit/s NRZ-OOK encoding of a dual-mode 850 nm VCSEL with a highly In-doped and small Zn-diffused emission area. *Photonics Res.* **2022**, *10*, 1602. [\[CrossRef\]](#)
21. Kao, H.-Y.; Tsai, C.-T.; Leong, S.-F.; Peng, C.-Y.; Chi, Y.-C.; Huang, J.J.; Kuo, H.-C.; Shih, T.-T.; Jou, J.-J.; Cheng, W.-H.; et al. Comparison of single-/few-/multi-mode 850 nm VCSELs for optical OFDM transmission. *Opt. Express* **2017**, *25*, 16347–16363. [\[CrossRef\]](#) [\[PubMed\]](#)
22. Cheng, C.-H.; Shen, C.-C.; Kao, H.-Y.; Hsieh, D.-H.; Wang, H.-Y.; Yeh, Y.-W.; Lu, Y.-T.; Huang Chen, S.-W.; Tsai, C.-T.; Chi, Y.-C.; et al. 850/940-nm VCSEL for optical communication and 3D sensing. *Opto-Electron. Adv.* **2018**, *1*, 180005. [\[CrossRef\]](#)
23. Song, D.-S.; Kim, S.-H.; Park, H.-G.; Kim, C.-K.; Lee, Y.-H. Single-fundamental-mode photonic-crystal vertical-cavity surface-emitting lasers. *Appl. Phys. Lett.* **2002**, *80*, 3901–3903. [\[CrossRef\]](#)
24. Danner, A.J.; Raftery, J.J., Jr.; Yokouchi, N.; Choquette, K.D. Transverse modes of photonic crystal vertical-cavity lasers. *Appl. Phys. Lett.* **2004**, *84*, 1031–1033. [\[CrossRef\]](#)

25. Lin, Y.-H.; Tsai, C.-T.; Wu, W.-L.; Cheng, C.-H.; Choquette, K.D.; Lin, G.-R. Photonic crystal structured multi-mode VCSELs enabling 92-Gbit/s QAM-OFDM transmission. *J. Light. Technol.* **2021**, *39*, 4331–4340. [[CrossRef](#)]
26. Shi, J.-W.; Chen, C.-C.; Wu, Y.-S.; Guol, S.-H.; Kuo, C.; Yang, Y.-J. High-Power and High-Speed Zn-Diffusion Single Fundamental-Mode Vertical-Cavity Surface-Emitting Lasers at 850-nm Wavelength. *IEEE Photonics Technol. Lett.* **2008**, *20*, 1121–1123. [[CrossRef](#)]
27. Chen, C.C.; Liaw, S.J.; Yang, Y.J. Stable single-mode operation of an 850-nm VCSEL with a higher order mode absorber formed by shallow Zn diffusion. *IEEE Photonics Technol. Lett.* **2001**, *13*, 266–268. [[CrossRef](#)]
28. Shi, J.-W.; Kuo, F.-M.; Hsu, T.-C.; Yang, Y.-J.; Joel, A.; Mattingley, M.; Chyi, J.-I. The Monolithic Integration of GaAs–AlGaAs-Based Untraveling-Carrier Photodiodes With Zn-Diffusion Vertical-Cavity Surface-Emitting Lasers With Extremely High Data Rate/Power Consumption Ratios. *IEEE Photonics Technol. Lett.* **2009**, *21*, 1444–1446. [[CrossRef](#)]
29. Tanigawa, T.; Onishi, T.; Nagai, S.; Ueda, T. 12.5-gbps operation of 850-nm vertical-cavity surface-emitting lasers with reduced parasitic capacitance by BCB planarization technique. *IEEE J. Quantum Electron.* **2006**, *42*, 785–790. [[CrossRef](#)]
30. Haglund, E.P.; Kumari, S.; Haglund, E.; Gustavsson, J.S.; Baets, R.G.; Roelkens, G.; Larsson, A. Silicon-Integrated Hybrid-Cavity 850-nm VCSELs by Adhesive Bonding: Impact of Bonding Interface Thickness on Laser Performance. *IEEE J. Sel. Top. Quantum Electron.* **2017**, *23*, 1700109. [[CrossRef](#)]
31. Kao, H.-Y.; Chi, Y.-C.; Tsai, C.-T.; Leong, S.-F.; Peng, C.-Y.; Wang, H.-Y.; Huang, J.J.; Jou, J.-J.; Shih, T.-T.; Kuo, H.-C.; et al. Few-mode VCSEL chip for 100-Gb/s transmission over 100 m multimode fiber. *Photonics Res.* **2017**, *5*, 507–515. [[CrossRef](#)]
32. Kuchta, D.M.; Rylyakov, A.V.; Doany, F.E.; Schow, C.L.; Proesel, J.E.; Baks, C.W.; Westbergh, P.; Gustavsson, J.S.; Larsson, A. A 71-Gb/s NRZ modulated 850-nm VCSEL-based optical link. *IEEE Photonics Technol. Lett.* **2015**, *27*, 577–580. [[CrossRef](#)]
33. Szczerba, K.; Westbergh, P.; Karlsson, M.; Andrekson, P.A.; Larsson, A. 70 Gbps 4-PAM and 56 Gbps 8-PAM using an 850 nm VCSEL. *J. Light. Technol.* **2015**, *33*, 1395–1401. [[CrossRef](#)]
34. Lavrencik, J.; Thomas, V.A.; Varughese, S.; Ralph, S.E. DSP-enabled 100 Gb/s PAM-4 VCSEL MMF links. *J. Light. Technol.* **2017**, *35*, 3189–3196. [[CrossRef](#)]
35. Xiong, F. M-ary amplitude shift keying OFDM system. *IEEE Trans. Commun.* **2003**, *51*, 1638–1642. [[CrossRef](#)]
36. Tsai, C.-T.; Peng, C.-Y.; Wu, C.-Y.; Leong, S.-F.; Kao, H.-Y.; Wang, H.-Y.; Chen, Y.-W.; Weng, Z.-K.; Chi, Y.-C.; Kuo, H.-C.; et al. Multi-Mode VCSEL Chip with High-Indium-Density InGaAs/AlGaAs Quantum-Well Pairs for QAM-OFDM in Multi-Mode Fiber. *IEEE J. Quantum Electron.* **2017**, *53*, 2400608. [[CrossRef](#)]
37. Dave, H.; Frysliie, S.T.; Schutt-Ainé, J.E.; Choquette, K.D. Modulation enhancements for photonic crystal VCSELs. *Proc. SPIE* **2017**, *10122*, 1012207.
38. 802.3bs-2017—IEEE Standard for Ethernet—Amendment 10: Media Access Control Parameters, Physical Layers, and Management Parameters for 200 Gb/s and 400 Gb/s Operation. Available online: <https://ieeexplore.ieee.org/document/8207825> (accessed on 12 December 2017).
39. Kasten, A.M.; Tan, M.P.; Leisher, P.O.; Choquette, K.D. Endlessly single-mode photonic-crystal vertical-cavity surface-emitting lasers. *Proc. SPIE* **2008**, *6908*, 69080B1.
40. Siriani, D.F.; Tan, M.P.; Kasten, A.M.; Lehman, A.C.; Leisher, P.O.; Sulkin, J.D.; Raftery, J.J., Jr.; Danner, A.J.; Giannopoulos, A.V.; Choquette, K.D. Mode control in photonic crystal vertical-cavity surface-emitting lasers and coherent arrays. *IEEE J. Sel. Top. Quantum Electron.* **2009**, *15*, 909–917. [[CrossRef](#)]
41. Yokouchi, N.; Danner, A.; Choquette, K. Two-dimensional photonic crystal confined vertical-cavity surface-emitting lasers. *IEEE J. Sel. Top. Quantum Electron.* **2003**, *9*, 1439–1445. [[CrossRef](#)]
42. Coldren, L.A.; Corzine, S.W.; Mašanović, M.L. *Diode Lasers and Photonic Integrated Circuits*; Wiley: New York, NY, USA, 2012.
43. Park, H.-G.; Hwang, J.-K.; Huh, J.; Ryu, H.-Y.; Kim, S.-H.; Kim, J.-S.; Lee, Y.-H. Characteristics of modified single-defect two-dimensional photonic crystal lasers. *IEEE J. Quantum Electron.* **2002**, *38*, 1353–1365. [[CrossRef](#)]
44. Zhang, Y.; Khan, M.; Huang, Y.; Ryou, J.; Deotare, P.; Dupuis, R.; Lončar, M. Photonic crystal nanobeam lasers. *Appl. Phys. Lett.* **2010**, *97*, 051104. [[CrossRef](#)]
45. Westbergh, P.; Gustavsson, J.S.; Kögel, B.; Haglund, Å.; Larsson, A. Impact of photon lifetime on high-speed VCSEL performance. *IEEE J. Sel. Top. Quantum Electron.* **2011**, *17*, 1603–1613. [[CrossRef](#)]
46. Haglund, E.; Haglund, Å.; Gustavsson, J.S.; Kögel, B.; Westbergh, P.; Larsson, A. Reducing the spectral width of high speed oxide confined VCSELs using an integrated mode filter. in SPIE 8276. In Proceedings of the Vertical-Cavity Surface-Emitting Lasers XVI, San Francisco, CA, USA, 7 February 2012.
47. Westbergh, P.; Gustavsson, J.S.; Haglund, Å.; Skold, M.; Joel, A.; Larsson, A. High-Speed, Low-Current-Density 850 nm VCSELs. *IEEE J. Sel. Top. Quantum Electron.* **2009**, *15*, 694–703. [[CrossRef](#)]
48. IEEE 802.3™ Industry Connections Ethernet Bandwidth Assessment. Available online: http://www.ieee802.org/3/ad_hoc/bwa/BWA_Report.pdf (accessed on 19 July 2012).
49. Lee, S.-Y.; Cheng, C.-H.; Tseng, H.-Y.; Chen, X.; Lo, W.-C.; Li, K.; Wang, C.-H.; Tsai, C.-T.; Kuo, H.-C.; Li, M.-J.; et al. Comparing the Dual-Mode VCSEL in OM4-MMF and GI-SMF Links for NRZ-OOK and 16-QAM-OFDM Transmissions. *IEEE Photonics J.* **2022**, *14*, 7927713. [[CrossRef](#)]
50. Lin, G.-R.; Kuo, H.-C.; Cheng, C.-H.; Wu, Y.-C.; Huang, Y.-M.; Liou, F.-J.; Lee, Y.-C. Ultrafast 2 × 2 green micro-LED array for optical wireless communication beyond 5 Gbit/s. *Photonics Res.* **2021**, *9*, 2077–2087. [[CrossRef](#)]

51. Papandreou, N.; Antonakopoulos, T. A new computationally efficient discrete bit-loading algorithm for DMT applications. *IEEE Trans. Commun.* **2005**, *53*, 785–789. [[CrossRef](#)]
52. Ling, W.A.; Lyubomirsky, I.; Rodes, R.; Daghighian, H.M.; Kocot, C. Single-Channel 50G and 100G Discrete Multitone Transmission With 25G VCSEL Technology. *J. Light. Technol.* **2015**, *33*, 761–767. [[CrossRef](#)]

Disclaimer/Publisher’s Note: The statements, opinions and data contained in all publications are solely those of the individual author(s) and contributor(s) and not of MDPI and/or the editor(s). MDPI and/or the editor(s) disclaim responsibility for any injury to people or property resulting from any ideas, methods, instructions or products referred to in the content.